Geophys. J. Int. (2006) **166,** 238–252 doi: 10.1111/j.1365-246X.2006.02965.x

Seismotectonic constraints at the western edge of the Pyrenees: aftershock series monitoring of the 2002 February 21, 4.1 Lg earthquake

M. Ruiz,[1] J. Díaz,[1] J. Gallart,[1] J. A. Pulgar,[2] J. M. González-Cortina[2] and C. López[2]

[1]*Dpt. Geofísica i Tectònica, Institut de Ciències de la Terra 'Jaume Almera' IJA-CSIC, Lluís Solé i Sabarís s/n,* 08028 *Barcelona, Spain. E-mail: mruiz@ija.csic.es*

[2]*Dpt. Geología, Universidad de Oviedo, Arias de Velasco s/n,* 33005 *Oviedo, Spain*

Accepted 2006 February 10. Received 2006 February 9; in original form 2005 February 15

SUMMARY

Seismic data recorded from a temporary network deployed at the western edge of the Pyrenees is used to study the aftershocks series following a magnitude 4.1 earthquake that took place on 2002 February 21, to the NW of Pamplona city. Aftershock determinations showed events distributed between 1 and 4 km depth in a small active area of about 4 km^2, E–W oriented delineating the southern sector of the Aralar thrust unit. This seismogenic feature is supported by focal solutions showing a consistent E–W nodal plane with normal faulting following the main strike-slip rupture. The Aralar structure with its shallow activity may be interpreted as a conjugate system of the NE–SW deep-seated Pamplona active fault nearby. Cross-correlation techniques and relative location of event clusters further constrained the epicentral domain to 2 km long and 1 km wide. Statistical relations and parameters established indicate a rather low *b*-value of 0.8 for the Gutenberg–Richter distribution, denoting a region of concentrated seismicity, and a *P*-parameter of 0.9 for the Omori's law corresponding to a low decay of the aftershock activity in this area. More than 100 aftershocks were accurately located in this high-resolution experiment, whereas only 13 of them could be catalogued by the permanent agencies in the same period, due to a much sparser distribution. The results enhance the importance of using dense temporary networks to infer relevant seismotectonic and hazard constraints.

Key words: aftershocks parameters, clustering analysis, Pamplona fault, seismicity, temporary array, western Pyrenees.

1 INTRODUCTION

On 2002 February 21 a magnitude 4.1 Lg (4.8 mb) earthquake took place in North Spain at the western edge of the Pyrenees, in the so-called Basque Cantabrian basin that marks the transition between the Pyrenean Chain and the Cantabrian Mountains. The Spanish National Geographical Institute (IGN) network located the epicentre near the Irurtzun village, less than 15 km NW from Pamplona city (Fig. 1). The event was widely felt in the region, with EMS intensity values from V at the vicinity of the epicentral area to III in Pamplona and Alsasua cities. This work deals with the analysis of the aftershock series, as recorded by a dense temporary network covering a circular zone of about 25 km of radius centred at the epicentre of the main event.

The region is characterized by a moderate and sparse seismicity, mainly concentrated westwards of Pamplona where events, distributed in depth between 5 and 20 km, are related to the central segment of the Pamplona Fault (Grandjean *et al.* 1994; Souriau & Pauchet 1998; Ruiz *et al.* 2006). This accident is a NE–SW-striking deep structure that runs from the Palaeozoic Basque Massifs to the Ebro Basin. It is only expressed at surface in its central segment, in the Pamplona basin, where a line of Triassic salt diapirs marks the fault trace (Martínez-Torres 1989; Turner 1996; Faci *et al.* 1997). Historical catalogues report three earthquakes felt with intensity VI in the Pamplona area during the end of the 19th and the beginning of the 20th centuries (Olivera & Gallart 1987; Ruiz *et al.* 2006). Instrumental catalogues show a present-day moderate to low-magnitude seismicity WNW of Pamplona city, in the study area, with magnitudes near 5 reported in past decades (see Ruiz *et al.* 2006). Between 1982 May and June a seismic crisis produced up to 28 earthquakes with magnitudes between 2.7 and 4.9 (Olivera & Gallart 1987). On 1996 February 25 and 1998 October 27, 4.5 and 4.8 magnitude earthquakes were also reported in the International Seismological Centre (ISC) and Observatoire Midi-Pyrénées (OMP) catalogues, respectively.

The origin of the Basque Cantabrian basin is related to the extensional period that leads to the opening of the Gulf of Biscay and the individualization of the Iberian Peninsula as a subplate. The extension was particularly intense during Aptian–Albian interval owing to transtensive movements related to the counter-clockwise rotation of

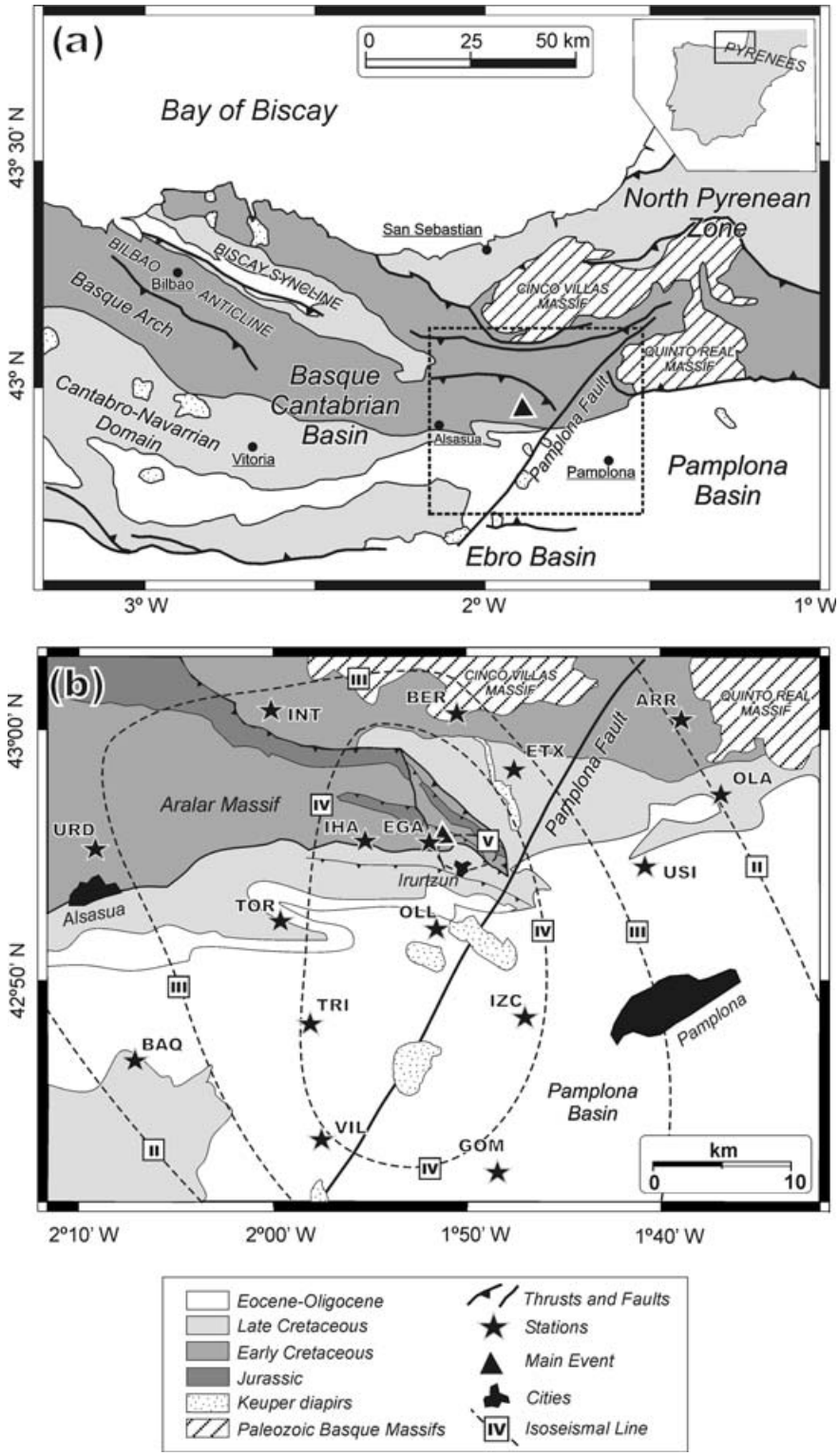

Figure 1. (a) Geological sketch of the study area. (b) Blow up of the area covered by the network (Geology modified from IGME 1978, 1987). The epicentre and isoseistes of the February 21 main event are shown. EMS intensity values of V were reported in the Irurtzun village for the IGN service.

Iberia with respect to stable Europe (Montadert *et al.* 1979; Rat 1988; García-Modéjar 1996). The eastern limit of the Basque–Cantabrian basin is usually placed at the Pamplona Fault (Fig. 1). This fault, also named Estella Fault, is a NE–SW crustal structure, which acted as a transfer zone during Cretaceous extension and played an important role in controlling the Mesozoic sedimentation.

During the Alpine (Pyrenean) orogeny in Tertiary times, the roughly N–S convergence of Iberia and Eurasia resulted in the closure of the Mesozoic basins and the formation of the Pyrenean Chain (Choukroune, 1992), leading to the inversion of the Basque–Cantabrian basin in the Palaeogene. The Pamplona fault, acted as a major traverse structure during the Alpine compression as

Table 1. Location and description of the instruments deployed during this experiment. The network geometry and the location of some continuous recording instruments was changed to improve the hypocentral determinations.

Station name	Recording period	Latitude (N)	Longitude (W)	Height (m)	Instrument	Recording mode	Sampling rate	Station correction (s)
GOM	02/02/22–02/03/13	42° 42.395′	1° 48.272′	592	Reftek	Continuous	100 sps	0.11
BER	02/02/22–02/03/29	43° 0.667′	1° 50.382′	814	Reftek	Continuous	100 sps	0.15
TRI	02/02/22–02/02/24	42° 48.314′	1° 57.981′	1000	MarsLite	Continuous	62.5 sps	0.18
OLL	02/02/22–02/03/29	42° 52.108′	1° 51.438′	555	MarsLite	Continuous	62.5 sps	0.10
USI	02/02/23–02/03/29	42° 54.577′	1° 40.632′	632	MarsLite	Continuous	62.5 sps	0.11
IHA	02/02/23–02/03/12	42° 55.632′	1° 55.142′	500	MarsLite	Continuous	62.5 sps	0.09
IZC	02/02/23–02/03/29	42° 48.572′	1° 46.843′	445	Mars88	Trigger	62.5 sps	0.08
VIL	02/02/24–02/03/12	42° 43.692′	1° 57.388′	622	MarsLite	Continuous	62.5 sps	0.11
	02/03/12–02/03/29				Mars88	Trigger	62.5 sps	
URD	02/02/24–02/03/29	42° 55.288′	2° 09.115′	593	Mars88	Trigger	62.5 sps	0.11
INT	02/02/24–02/03/12	43° 0.828′	2° 0.010′	420	Mars88	Trigger	62.5 sps	0.08
	02/03/12–02/03/28				MarsLite	Continuous	62.5 sps	
BAQ	02/02/25–02/03/29	42° 46.857′	2° 07.068′	664	Mars88	Trigger	62.5 sps	0.12
ETX	02/02/25–02/03/12	42° 58.29′	1° 47.284′	420	Mars88	Trigger	62.5 sps	0.08
	02/03/12–02/03/29				MarsLite	Continuous	62.5 sps	
EGA	02/03/13–02/03/28	42° 55.544′	1° 51.808′	536	Reftek	Continuous	100 sps	0.10
OLA	02/03/13–02/03/29	42° 57.445′	1° 36.698′	591	Mars88	Trigger	62.5 sps	0.11
ARR	02/03/13–02/03/29	43° 00.417′	1° 38.746′	602	Mars88	Trigger	62.5 sps	0.11
TOR	02/03/14–02/03/29	42° 52.415′	1° 59.520′	596	Mars88	Trigger	62.5 sps	0.11

evidenced by the strong lateral changes of the crustal structure on both sides of the fault (Pedreira *et al.* 2003). This fault has been classically interpreted as a major strike-slip fault with either sinistral (Engeser & Schwentke 1986; Rat 1988; Faci *et al.* 1997), dextral (Müller & Rodgers 1977; Turner 1996) or combined (Martínez-Torres 1989) sense of movement. More recently, the absence of significant palaeomagnetic rotation around the fault has supported a new interpretation of the Pamplona Fault as a hanging-wall drop fault resulting from variations of the geometry and thickness of Mesozoic sequences on both sides of the fault (Larrasoaña *et al.* 2003).

Two domains have been classically defined within the Basque–Cantabrian basin (Feuillée & Rat 1971), the Basque Arch at the northern part, with a northward vergence and a significant structural complexity and the Cantabro-Navarrian Domain to the South, with a general South vergence of structures. The epicentral zone here considered is located at the Aralar range, one of the subdomains of the Basque Arch, situated in the eastern prolongation of the Bilbao Anticline and characterized by several north-directed thrust sheets.

2 DATA ACQUISITION AND PROCESSING

From 2002 February 22 to March 29, a dense temporal network composed by a total of 16 stations was deployed in the epicentral zone (Fig. 1 and Table 1). Up to 13 stations were operated at the same time with epicentral distances lower than 25 km. Reftek, MarsLite and Mars88 digital dataloggers were used in this experiment. A total of six instruments worked in continuous recording mode, while the other seven operated in triggered mode. All the stations were equipped with Lennartz three-component 1 Hz seismometers. As first accurate hypocentral locations of the aftershocks series were obtained, the network geometry was modified to improve the coverage of the active zone.

Events from the published catalogues of IGN, RENASS (Pyrenean French network) and CEA (French's Atomic Energy Commission) networks were extracted from the data set obtained during this temporary experiment. From February 21 to March 18

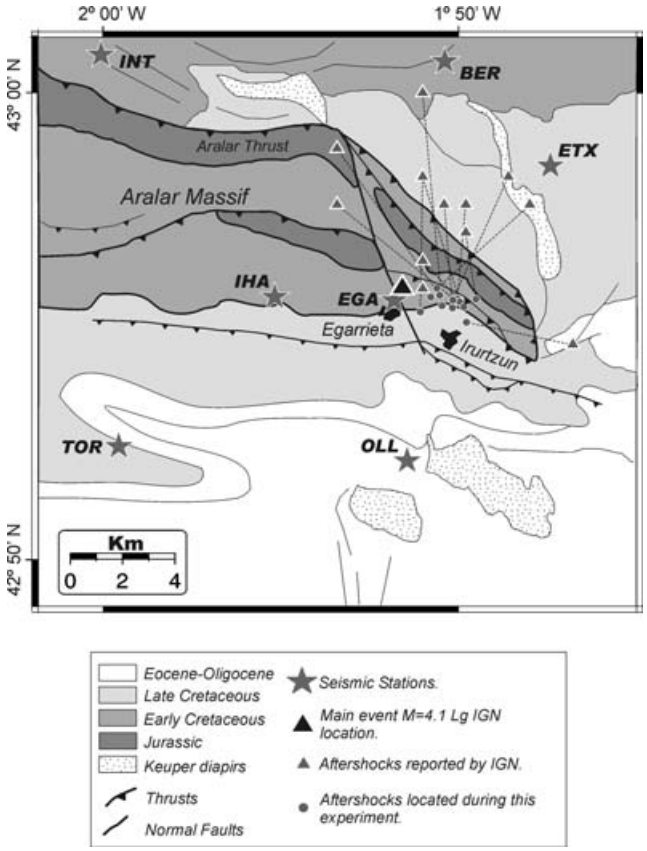

Figure 2. Epicentral determinations of the aftershocks reported by the IGN service (triangles) and relocations using data from permanent and temporary networks (circles). (Geology modified from IGME 1978, 1987).

the IGN service reported 13 earthquakes following the main event, with magnitudes between 1.8 and 3.5, sparsely located in the Pamplona Region (Fig. 2). The RENASS network reported only five of these earthquakes, with magnitudes between 2.6 and 3.7, and the

Table 2. *P*-velocity model used for hypocentre inversion.

Depth Z (km)	V_P (km s^{-1})
0.0	5.5
3.0	6.0
12.5	6.2
22.0	6.7
38.0	8

CEA catalogue contains 11 events with magnitudes between 2 and 4.1. All these events were relocated using the additional information provided by our network.

A STA/LTA detection algorithm was applied to the data of each of the stations operated in continuous mode, and the events detected by the triggered stations were also included in the detection lists. An event was retained only if it was present on 3 or more stations in an 8 s time interval. A total of 319 uncatalogued aftershock events were detected using this method, and up to 106 events from this set of quakes had enough station coverage to be correctly located.

3 HYPOCENTRAL DETERMINATIONS AND FOCAL MECHANISMS

Phase picking and seismogram processing was done using SAC (Seismic Analysis Code) package (Goldstein & Minner 1996; Goldstein *et al.* 2003). First hypocentral determinations were obtained from the Hypo71 code (Lee & Lahr 1975), using a homogeneous five-layered velocity-depth model derived from wide-angle seismic profiles across the Basque–Cantabrian basin (Pedreira *et al.* 2003) (Table 2). A time correction is considered for each station to take into account their altitude (Table 1).

The epicentres of aftershocks reported by IGN, RENASS and CEA seismological services show a sparse distribution probably related to the low station coverage of this region. Relocations of these aftershocks were done using together the phase picking of temporary and permanent seismic networks. The relocations clearly improved the resolution on the epicentral zone, grouping all the sparse events closer to the main event, around Egarrieta village (Fig. 2).

The epicentres of the 93 new events identified and located in this experiment concentrate also at the same area, defining an epicentral zone of less than 4 km^2 (Fig. 3a), most of the events being distributed between 1 and 4 km depth (Fig. 3c). The mean quality *Q* obtained for these locations is always A or B, due to the dense network coverage. The results obtained have a mean rms value of 0.08 s and it is always lower than 0.2 s. The mean horizontal and vertical errors are 0.3 and 0.7 km respectively. The gap has a mean value of 113° and is always lower than 200°, showing two peaks corresponding to the two stages of the network (Fig. 4).

The accurate locations reveal a direct structural relation of this seismicity with the southeastern edge of the Aralar thrust sheets (Figs 3a and b), which could not have been inferred from permanent network determinations (Fig. 2). This unit, approximately 30 km long and up to 10 km wide, is situated at the eastern prolongation of the Bilbao Anticline. It is composed of Jurassic and Early Cretaceous carbonated terrains disposed along a general E–W direction and forming a north-verging thrust imbricate (Fig. 3b). Towards its eastern edge, the Egarrieta Fault, with a NNW–SSE direction and a dextral component, crosses all the structure and the thrust direction changes to the SE, probably affected by the NE–SW Pamplona fault (Martínez-Torres 1989; Faci *et al.* 1997).

Fault plane solutions of the main event and of the aftershocks with best azimuthal coverage (12 events with gaps less than 100° and at least six *P*-polarities were retained) have been computed using the FPFIT algorithm (Reasenberg & Oppenheimer 1985) (Fig. 5 and Table 3). The focal mechanism of the main event has been derived using 13 *P*-wave polarity readings from permanent networks, resulting in a dextral strike-slip solution with one of the nodal planes oriented N23W (Figs 3a and 5). The strike and rake uncertainties are equal to 5 degrees and zero for the dip error. The most common solution obtained for the aftershocks shows a normal fault with some strike-slip component, having one nodal plane oriented ENE–WSW (Figs 3a, d and 5). The average errors on the maximum likelihood solutions remained less than 20° for strike, dip and rake, respectively. The accuracy of these solutions was checked by analysing different parameters provided by the FPFIT package to assess the quality of the results. An estimation of the misfit of the solution is provided by the *F*-value ($F = 0$ representing a perfect fit to the data and $F = 1$ a complete misfit), which is in our case lesser than 0.15. Solutions are robust for station distribution ratio (STDR) greater than 0.5, and in our case it is comprised between 0.50 and 0.71. Hence, the solutions obtained appear to be stable and robust, even if in some particular cases small variations in the fault plane orientations can not be excluded.

The aftershock mechanisms suggest that after the main rupture as a shear fault, there has been a readjustment of the E–W thrusts in terms of normal fault movements. The local stress field is marked by maximum *P* directions oriented NW–SE (Table 3).

Possible directional dependences in the hypocentral depths distribution were tested by cross-sections over the Aralar structure in different directions (Fig. 3c). Hypocentres are mainly distributed between 1 and 4 km depth, and no clear dipping structures are observed. A geological cross-section with a N–S orientation was performed. The projection of the hypocentres over this cross-section shows as the events are related to the southern E–W thrusts slices of the Aralar structure (Fig. 3b).

The location of the main event over the NNW–SSE Egarrieta fault (Fig. 2) and the focal mechanism obtained, strongly suggest that a dextral movement of this N–S fault, generating a compressional stress field in the eastern sector of the Aralar edge, is the origin of this seismic crisis. Both the accurate location of the aftershocks, with an E–W distribution, and the focal solutions obtained for the most significant events, mainly normal fault solutions, suggest that the aftershocks are due to a relaxation process of the E–W thrusting slices after the main event.

4 STATISTICAL PARAMETERS OF THE AFTERSHOCKS

The data recorded by the two stations closer to the epicentral area (EGA and OLL, see Fig. 2) have been specifically analysed. All the detections resulting from STA/LTA algorithms were extracted for these two stations, revealing a set of additional events that were beyond the detection capacity of the whole network. During the 36 days of the experiment, the OLL station detected 511 aftershocks, whereas the algorithm for the whole network resulted in 319 events. The EGA station was operated only for the last 15 days, but up to 279 aftershocks were detected there in that period.

These additional data have been used to better constrain the evolution of the seismic series, including the characterization of the time decrement of the seismic activity and its frequency–magnitude distributions.

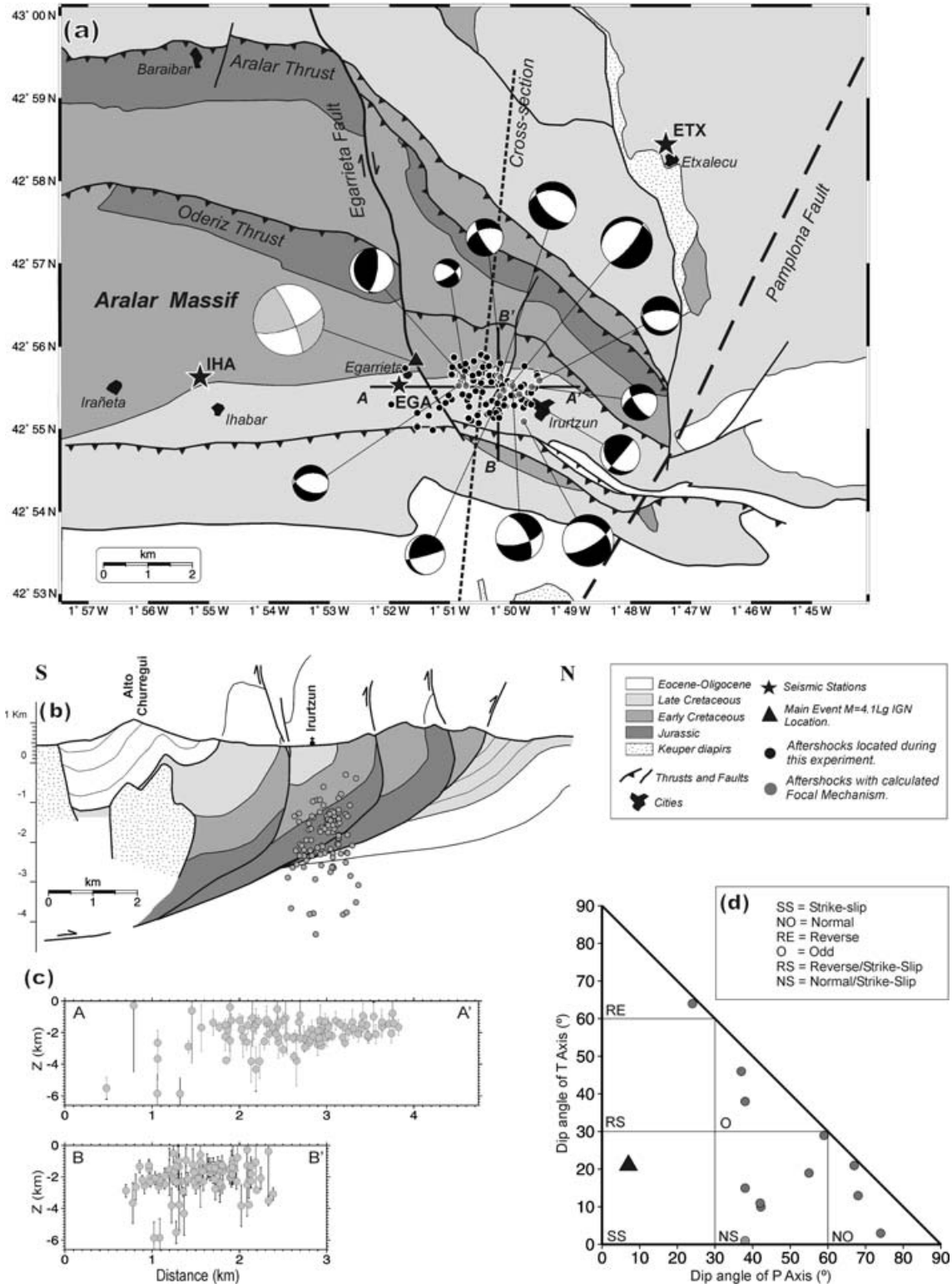

Figure 3. (a) Epicentral locations and fault plane solutions obtained. (Geology modified from IGME 1978, 1987) (b) Geological cross-section, approximately in a N–S direction. (c) Cross-sections over the Aralar structure, showing events distributed between 1 and 4 km depth. (d) Dip angle of *T*-axes versus dip angle of *P*-axes for the 13 fault plane solutions obtained.

4.1 Temporal evolution of the seismicity

Fig. 6(a) shows the temporal evolution of the seismicity as detected by the network. During the first operating period, from February 22 to March 12 (Julian days 53–71), the expected aftershock exponential decrease is not clearly imaged from the whole network (Fig. 6a), because most of the low-magnitude events were not recorded in the nearby stations operated in triggered mode. This decrease is better imaged at the OLL station, near the epicentral zone and equipped with a continuously recording device (Fig. 6b).

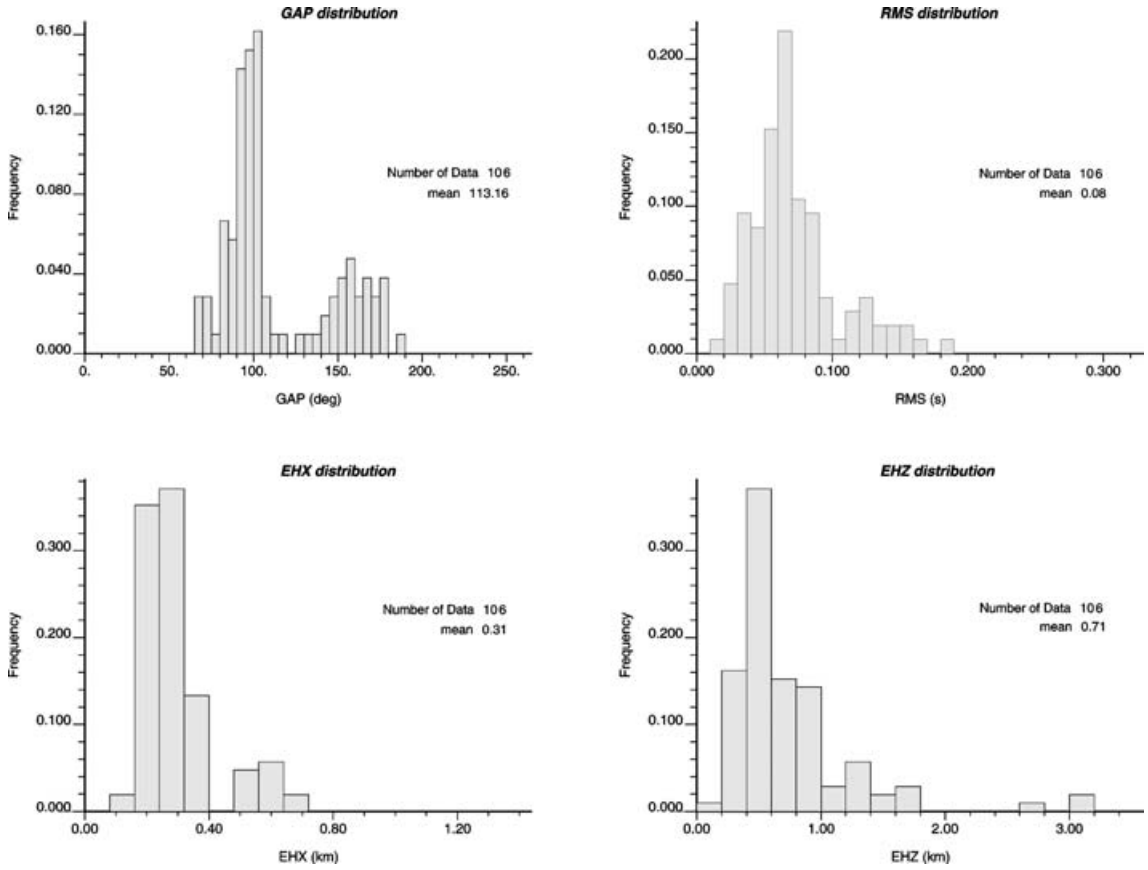

Figure 4. Error analysis of the hypocentral determinations obtained using Hypo71 program. The horizontal and vertical errors, Gap and RMS are shown.

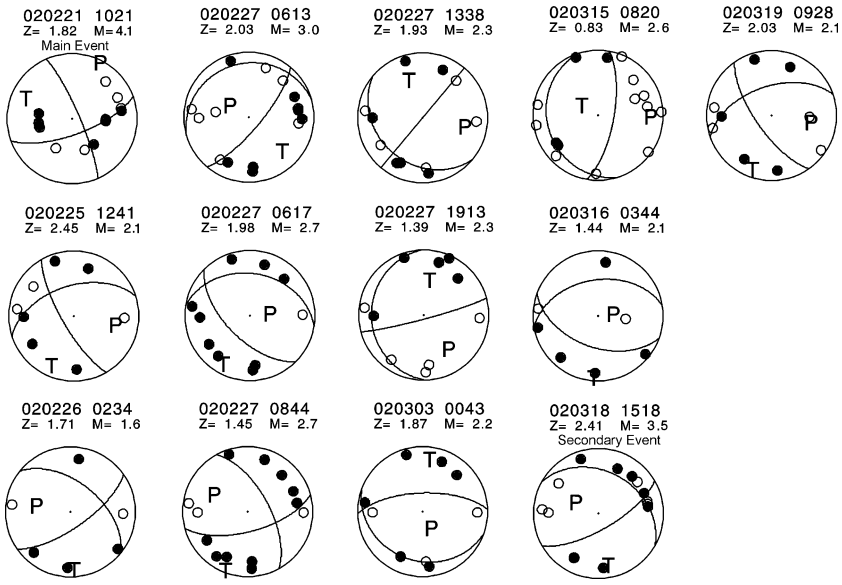

Figure 5. Fault plane solutions (lower hemisfere equal-area projection) of the 13 studied events. For each mechanism the date (year, month, day), the origin time (hour and minute), the focal depth in km (z) and the magnitude (M) are reported. P and T denote the P- and T-axes positions. Open circles and black dots indicate dilatations and compressions, respectively.

In the second part of the experiment, from March 13 to March 29 (Julian days 72–88), the detection threshold of the network was improved after the stations redistribution. The most significant observation is an abrupt increment of the seismicity related to the March 18 magnitude 3.5 event. The aftershock sequence triggered by this secondary event, with the characteristic exponential frequency distribution, is best imaged at EGA station that recorded up to 225 events (Fig. 6c), 139 of them also recorded at OLL station.

Table 3. Focal solutions obtained. FM: Number of polarities used in the inversion. The strike (Strk) and dip (Dip) angles for each plane, as well as the azimuth (Azm) and plunge (Plng) angles of the *P*- and *T*-axes, are reported. All the angles expressed in degrees.

Date	Origin	Latitude	Longitude	Depth	Mag	FM	Plane 1		Plane 2		*P*-axis		*T*-axis	
	Time	(°N)	(°E)	(km)			Strk	Dip	Strk	Dip	Azm	Plng	Azm	Plng
02/02/21	10:21:49	42.9300	−1.8600	1.82	4.1	13	70	70	337	81	25	7	292	21
02/02/25	12:41:47	42.9243	−1.8352	2.45	2.1	8	150	75	252	52	104	38	206	15
02/02/26	02:34:37	42.9253	−1.8455	1.71	1.6	6	55	70	309	53	278	42	178	11
02/02/27	06:13:46	42.9258	−1.8327	2.03	3.0	15	40	75	254	18	296	59	138	29
02/02/27	06:17:15	42.9270	−1.8360	1.98	2.7	10	135	60	279	36	86	68	211	13
02/02/27	08:44:27	42.9253	−1.8327	1.45	2.7	13	75	65	331	63	294	38	203	1
02/02/27	13:38:25	42.9235	−1.8308	1.93	2.3	11	130	30	40	90	103	38	337	38
02/02/27	19:13:38	42.9232	−1.8362	1.39	2.3	10	75	85	178	21	147	37	6	46
02/03/03	00:43:23	42.9263	−1.8252	1.87	2.2	9	110	25	268	67	161	67	5	21
02/03/15	08:20:48	42.9270	−1.8463	0.83	2.6	15	10	70	163	22	92	24	296	64
02/03/16	03:44:41	42.9253	−1.8475	1.44	2.1	7	110	50	260	44	85	74	186	3
02/03/18	15:18:53	42.918	−1.8295	2.41	3.5	14	60	70	299	36	292	55	172	19
02/03/19	09:28:41	42.925	−1.8273	2.03	2.1	9	145	70	251	53	102	42	202	12

The occurrence rate of aftershocks sequences is empirically described by the modified Omori formula:

$n(t) = K(C + t)^{-P}$ (Utsu 1961),

where $n(t)$ is the frequency of aftershocks per unit time (days) after the main shock. P is a rate constant for aftershocks decay, independent on the magnitude of the main event but reflecting mechanical conditions of the crust on a regional scale (Ogata 1999; Utsu 2002). Usual values for P lie between 0.7 and 1.8 (Kisslinger & Jones 1991; Guo & Ogata 1997). Constant C is related to the incompleteness of recordings immediately following the main shock (Hauksson & Jones 1989; Utsu 2002) and often shows strong dependence on magnitude of the main event. Constant K is also dependent on the magnitude of the main event and on the total number of quakes in the sequence (Kisslinger & Jones 1991).

This expression was fitted by a least-square method to obtain the constant K and the P parameter for the aftershocks of the magnitude 3.5 earthquake of 2002 March 18, as recorded at EGA station (Fig. 6c). We assumed in this case $C = 0$ as the station is located in the vicinity of the epicentral zone and was operating prior to the event. We obtained a constant K equal to 32 ± 1 with a P-value of 0.9 ± 0.2 (Fig. 6d), that is in the lower range of the expected values, indicating a moderate to low decay of the aftershocks in the southeastern edge of the Aralar region.

4.2 Local magnitudes and Gutenberg–Richter distributions

In order to fix the magnitudes of the aftershock events, we first established a local magnitude (M_D) formula, defined as an empirical relationship involving epicentral distance and total signal duration. We have used a relation of the form (Lee *et al.* 1972; Ruiz *et al.* 2006):

$M_D = a + b \operatorname{Log} T + cD,$

where T is the total signal duration in seconds, D is the epicentral distance in kilometres and a, b and c are constants determined statistically. The signal duration and the epicentral distances obtained at each station for the 13 events catalogued by the IGN service, with their known local magnitudes, were used to adjust the coefficients of the formula in a least-squares analysis. This resulted in the following equation, with a correlation coefficient of 94 per cent:

$M_D = -1.983 + 2.573 \operatorname{Log} T + 0.0312\ D$

Fig. 7 shows the local magnitude distributions of the earthquakes detected by the whole network, and by OLL and EGA stations respectively. For the events detected in those stations but not accurately located, we used for parameter D an average of the distance from the station position to the midpoint of the epicentral area, considering that it extends less than 4 km^2. EGA station, nearest to the epicentral zone, detected events with magnitudes between −1.2 and 3.5, while at OLL station, distant around 6.5 km, magnitude detection threshold was −0.4. For the whole network, the detection threshold was 0 for the first recording period, and improved to −0.4 for the second one. After the March 18 earthquake, a great amount of low-magnitude earthquakes were recorded in all the stations nearby.

The catalogues of the two closer stations EGA and OLL were also used to obtain, after a linear regression adjustment, the b-value of the cumulative Gutenberg–Richter distribution:

$\operatorname{Log} N = a - bM,$

where N is the total number of events with magnitude greater than M.

A statistical analysis of the b slope variability was performed testing different intervals of magnitude increments, and a stable solution was always obtained. A mean b-value of 0.78 ± 0.02 was inferred at EGA station using the 225 events following the March 18 event, considering magnitude increments of either 0.25, 0.2, 0.15 or 0.1. At OLL station, a mean b-value of 0.81 ± 0.02 was obtained using the complete catalogue, 511 events, and for the same magnitude discreteness (Fig. 8). The error bar of both calculations includes the statistical error from least-squares fitting, and the b-value variations due to magnitude increment.

The b coefficient is normally close to 1, but it may range between 0.5 and 1.5 depending on the region (Guo & Ogata 1997; Nanjo *et al.* 1998; Utsu 1999). The fractal dimension, D, of the active fault system involved in the seismic process is related to the b-value by a simple relationship: $D = 2b$ (Turcotte 1992; Guo & Ogata 1997). Therefore, low b-values are characteristic of regions with concentrated seismicity and well-defined fault planes (Njike-Kassala *et al.* 1992). The dimension $D = 1.6$ obtained in our study shows a

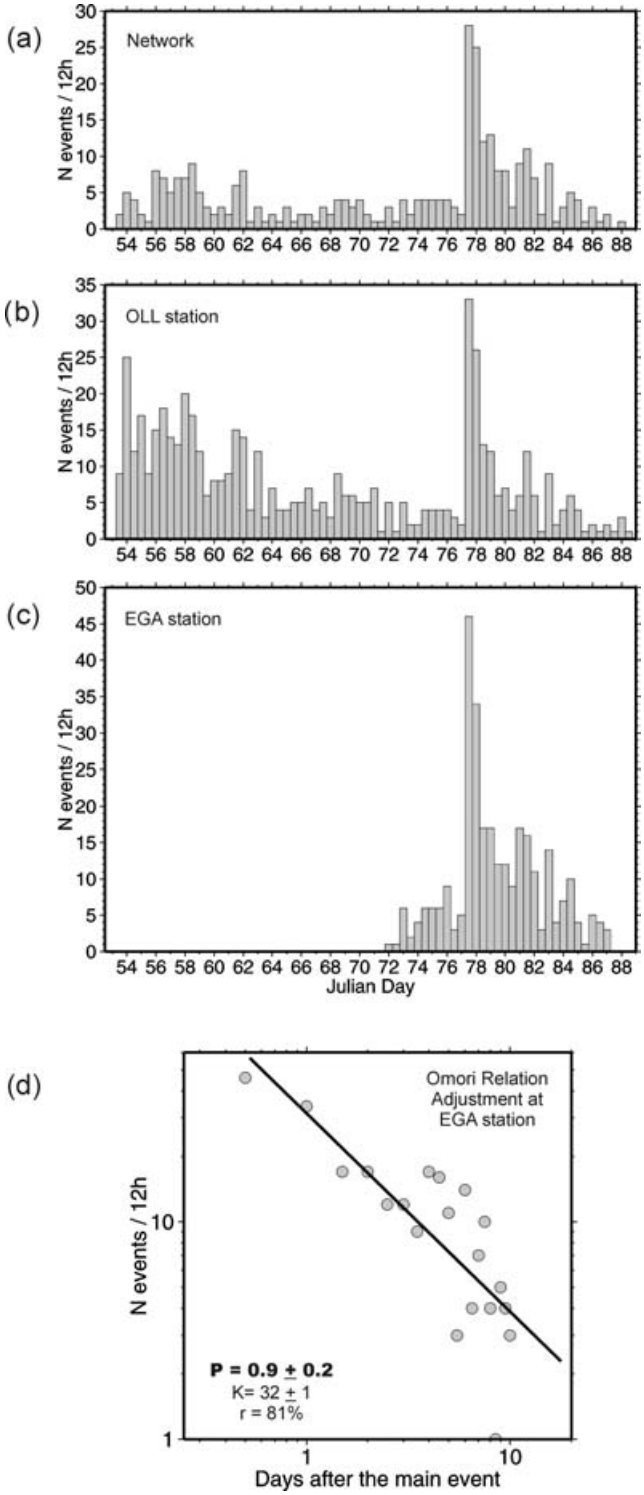

Figure 6. (a) Frequency distribution of events obtained by the detection algorithms applied to the whole network. (b) Same at OLL station, 6.5 km southwards from the epicentral zone, (c) Same at EGA station, only 1.9 km westwards from the epicentral area. (d) Adjustment of the *P*-parameter of the modified Omori relation at EGA station. The frequency $n(t)$ is computed as the number of events every 12 hr, and t is the time after the main event.

geometry intermediate between a line and a plane, corresponding to a well-defined hypocentral zone located in a small area of about 4 km^2 around the southern thrusts of Aralar system, with depths not exceeding 4 km.

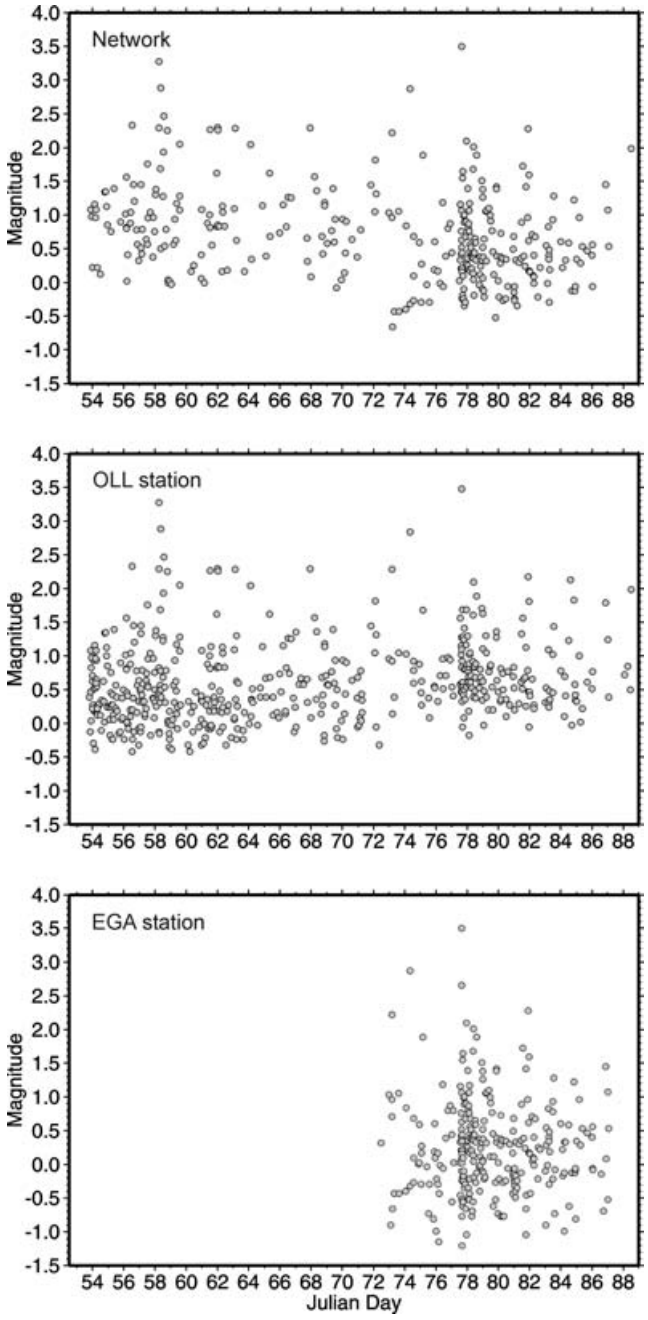

Figure 7. Time distribution of local magnitudes of the earthquakes detected with the whole network, and at OLL and EGA stations respectively.

The b value resulting from this experiment is lower than the one obtained by Njike-Kassala *et al.* (1992) in another area of the western Pyrenees near the Pamplona Fault: $b = 0.96 \pm 0.1$, the activity of which is sparser in comparison with the one related to the Aralar structure.

5 CLUSTERING ANALYSIS

Aftershocks sequences are often characterized by numerous events with striking waveform similarities at individual stations, usually referred to as clusters or earthquake families. The source–time function, propagation path, station site and recording instruments are factors contributing to the seismogram similarity in a given

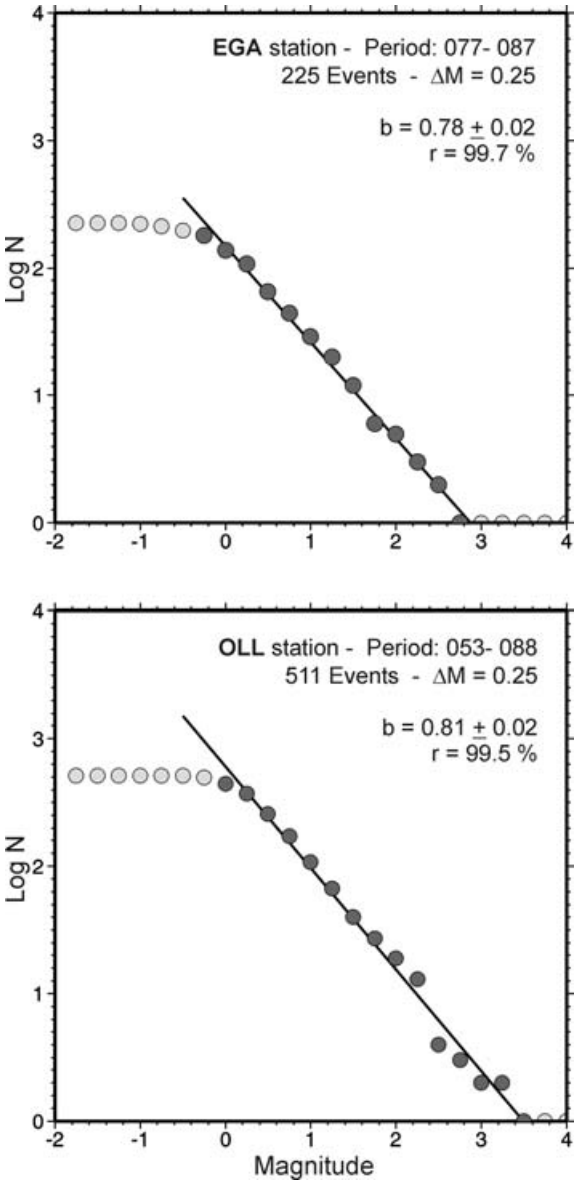

Figure 8. Cumulative Gutenberg–Richter distribution and *b*-value fitting using 0.25 magnitude increments at EGA and OLL stations. EGA catalogue holds the events related to the 3.5M_L secondary event while OLL station began recording in February, 22 and holds part of the aftershocks of the main event.

station (Tsujiura 1983; Poupinet *et al.* 1984; Maurer & Deichmann 1995). Therefore, clustering analysis can only be performed if the epicentral zone is narrow compared to the dimensions of near-source heterogeneities and to the observed wavelengths (Maurer & Deichmann 1995). The detection of each of these clusters can give some clues to the understanding of the whole rupture and relaxation processes.

The high waveform similarity of events of a given cluster may also be used to highly improve the picking of the phase onsets, allowing an accurate relative hypocentre determination that can provide enhanced resolution on the location and extent of the seismotectonic structure (Frémont & Malone 1987; Deichmann & García-Fernández 1992; Got *et al.* 1994; Augliera *et al.* 1995; Shearer 1997; Rubin *et al.* 1999; Saccorotti *et al.* 2002).

5.1 Cluster detection

The algorithm described by Maurer & Deichmann (1995), based on correlation analysis of *P*- and *S*-wave data, was applied to detect and associate events with similar waveforms. In this approach, the event cluster separation is achieved by close inspection of row patterns in the correlation matrix, avoiding a typical problem of the Equivalence class method (Aster & Scott 1993), which could result in events belonging to different clusters.

The waveform similarity is checked station per station for *P* and *S* waves. *S*-wave data provides a more reliable measure of similarity than *P*-wave data, as their waveforms are generally more complex than the first arriving *P* wavelets (Maurer & Deichmann 1995). However, *P*-wave correlation must also be done to verify the consistency of the onset polarities.

Events belonging to the same cluster should exhibit similarities, station per station over the whole network, but stations located close to the epicentral area with good signal-to-noise ratio will give higher correlation coefficients. Therefore, seismograms from OLL station were used in our cluster search, although consistency was always guaranteed by stations BER and USI, which also recorded all the 106 retained earthquakes. A 3–15 Hz bandpass filter was applied prior to the correlation analysis to improve the semblance of the time-series. The normalized cross-correlation among all the independent pair of signals was finally calculated for *P* and *S* waves. *P*-wave cross-correlation matrix was obtained correlating a time window of 1 s, starting 0.25 s before the *P* phase picked, and the *S*-wave cross-correlation matrix resulted from the correlation of 2 s, from the N–S channel, starting 0.15 s before the *S* picking. A cross-correlation threshold of 85 per cent was imposed to the time-series, hence only events with a correlation coefficient in *S* and *P* waves higher than 0.85 were kept to perform the cluster separation.

Using these parameters, up to 10 multiplets or clusters were found in our data set, containing at least three similar earthquakes. In total, they group 59 events, 55 per cent of the 106 events revised. Most of the earthquakes in each family occur through all the recording period without any relevant temporal distribution, except families G and H the events of which concentrate in 3 days, both between March 18 and 20. Fig. 9 shows the vertical component seismograms of the 10 families recorded at OLL. Most of the families show an impulsive *P* arrival, except families F, G and H, which have an emergent *P* onset. Clusters C, J and I show a strong secondary arrival approximately 0.5 s after the *P* onset. The *S* wave arrivals show, for all the families, a maximum of amplitude for frequencies between 7–8.5 Hz. Clusters B, C, F and H also show strong amplitude peaks for frequencies of 11, 13 and 16 Hz.

5.2 Relative event relocation using waveform similarity

Events with high waveform similarities allow for a very precise determination of the arrival time differences for a same phase. These time differences can be calculated using either the cross-spectral analysis method (Poupinet *et al.* 1984; Frémont & Malone 1987; Got *et al.* 1994; Rubin *et al.* 1999), or the time-domain, cross-correlation approach (Deichmann & García-Fernández 1992; Augliera *et al.* 1995; Saccorotti *et al.* 2002), which is used in this study. In both approaches, cross-correlation functions are calculated to obtain the time-shift between pair of signals, improving the precision of the relative arrival time estimations.

For each family, the event recorded by the greatest number of stations, usually the highest magnitude earthquake, was selected as

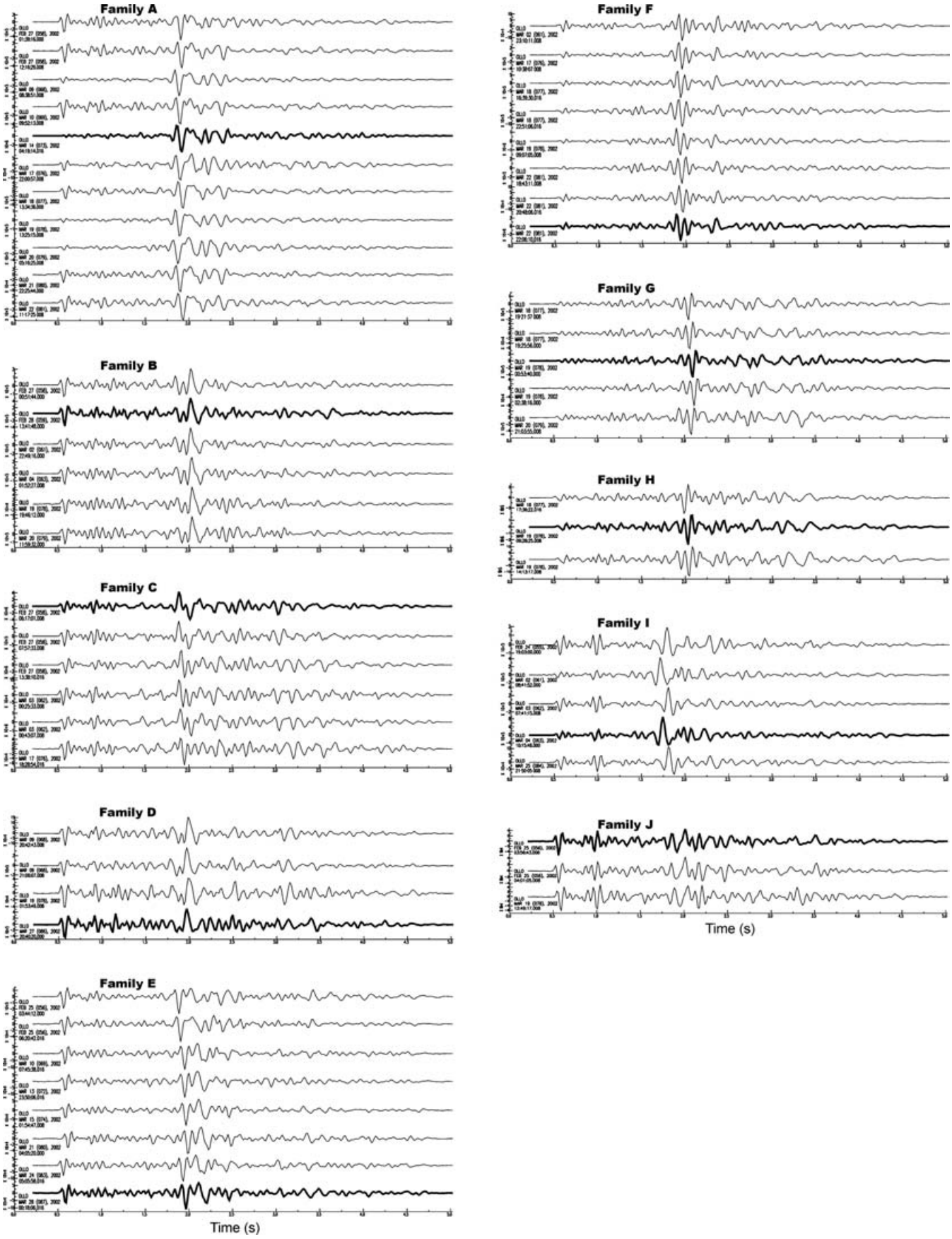

Figure 9. Vertical component seismograms, 3–15 Hz bandpass filtered, recorded at OLL station, of the ten families obtained by correlation analysis. Bold traces are the master events used to cluster event location.

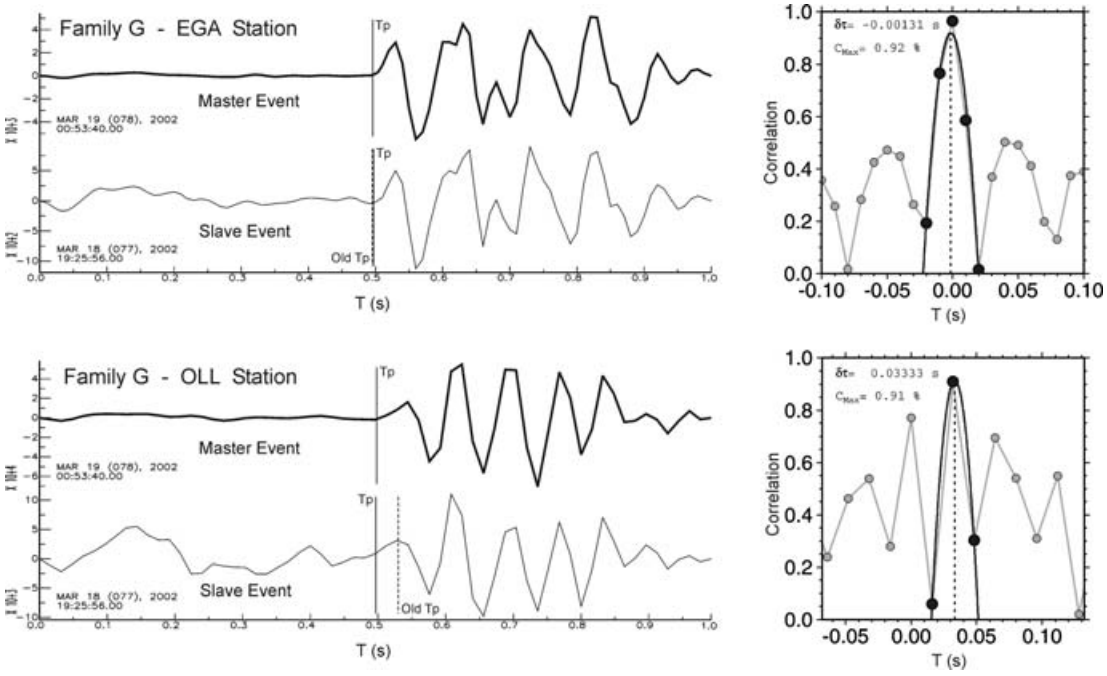

Figure 10. Pairs of master and slave events of the G cluster, 3–15 Hz bandpass filtered, recorded at EGA and OLL stations and their discrete cross-correlation functions, indicated by grey and black dots. Each pair of seismograms is aligned according to the maximum of their cross-correlation function and the original and calculated *P* onsets are shown for each slave event. The continuous bold curves show the parabolic function fitted through the convex part of the maximum peak of the discrete cross-correlation function. The maximum of the interpolated cross-correlation function is indicated by a discontinuous vertical line and allows the retrieval of the time-shift between onsets of master and slave events.

the master event. Its phase picking were then used as a reference to correct the onsets of the slaves events of its family.

As signal to noise ratio at far-off stations and low-magnitude events can sometimes be moderate, the time-shift was estimated by fitting a parabolic function, with a least-squares method, through the discrete points that form the convex part of the maximum peak of the cross-correlation curve (Deichmann & García-Fernández 1992; Augliera *et al.* 1995). A time window of 1 s, starting 0.5 s before the *P* phase picked during the location procedure, was used to obtain the discrete cross-correlation functions needed to correct the *P* onsets of the slave events (Fig. 10). The *S* onsets corrections were obtained using time windows of 2 s starting 1 s before the *S* phase picked. The interpolation of the cross-correlation curve provides a time-shift measure between the traces smaller than the sampling interval.

The results obtained in this way may be influenced by the confidence of the phase picking of the master event and its signal semblance with the slave one. Repeating the correlations with all possible pairs of events within a given set, and applying a least-squares fitting procedure, it is possible to determine arrival-time differences between master and slaves events, which minimize discrepancies, allowing a more precise determination on the onset times (see Deichmann & García-Fernández 1992 and Saccorotti *et al.* 2002 for the mathematical formulation of the procedure). Consistency among the synchronization of all the stations was always insured by GPS or DCF systems, and simplifications proposed by Saccorotti *et al.* (2002) were applied.

The relocation of the event clusters was performed following two schemes. First, the relative location procedure was applied following a classical master event approach. The earthquakes defined as master events were located using the standard Hypo71 program. Then the arrival times of the slave events were corrected with the time-shifts, calculated by cross-correlation, and the travel time residuals resulting from the master event localization, which are handled as a new station correction (Deichmann & García-Fernández 1992; Saccorotti *et al.* 2002). Finally the corrected arrivals of the slave events are inverted, obtaining their relative positions to the master events (Fig. 11). Relative locations of the cross-correlated event families were also performed with the double-difference hypocentre locations approach (Waldhauser & Ellsworth 2000), using the HypoDD program (Waldhauser 2001).

Fig. 11(a) shows the standard locations of the event families without any correction, to be compared with improved locations which display the slave events clustered around their master event (Figs 11b and c). The relocated events, particularly those with the double difference approach constrain a much narrower epicentral area (Fig. 11c). A well-defined E–W region of about 2 km long and less than 1 km wide is imaged, which follows the southern thrusting slice delineating the southern sector of the north-verging Aralar thrusting system. The depth range appears also better constrained, with most of the events located between 1.5 and 2 km depth.

The hypocentral distributions imaged in N–S and E–W cross-sections (Figs 11b and c) probably delineate the sectors of the fault that have been active and which could not be resolved with the standard locations (Fig. 11a). The E–W cross-sections (A-A′ in Figs 11b and c) show a thin discontinuous E–W pattern in which two groups of events can be distinguished. The westernmost one is formed by families A, I and J, distributed mainly in a thin line at 1.5 km depth, but with a few events reaching the surface. The other families, in the eastern fault sector, are distributed at 1.5 to 2 km depth, although some events may extend to 4 km depth. The N–S cross-sections (B–B′ in Figs 11b and c) suggest a southward-dipping distribution, specially in the southern half of the transect where the events lay from near the surface down to 4 km depth, which may delineate the fault plane responsible of the seismic crisis.

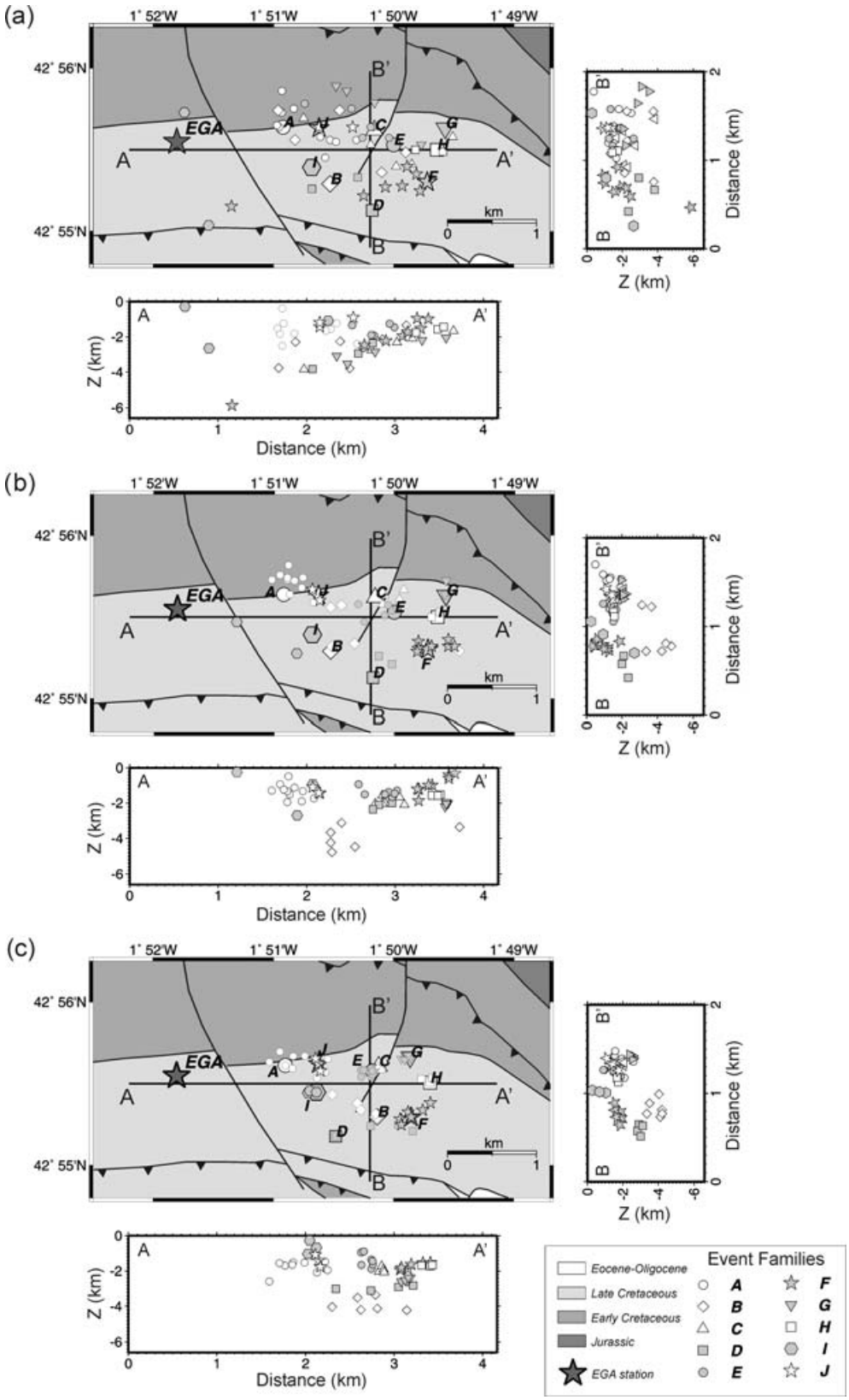

Figure 11. (a) Standard absolute locations of the events belonging to the ten families obtained. Master events are indicated with a symbol greater than slave events and marked with the label of each family. Two, N–S and E–W, cross-sections show the distribution in depth of these events. (b) Relative locations of the ten earthquake families obtained from cross-correlation and using the master event approach technique. All the earthquakes appearing in this figure have mean quality *Q* equal to A or B. (c) Relative locations of the cross-correlated events obtained using Double Difference approach.

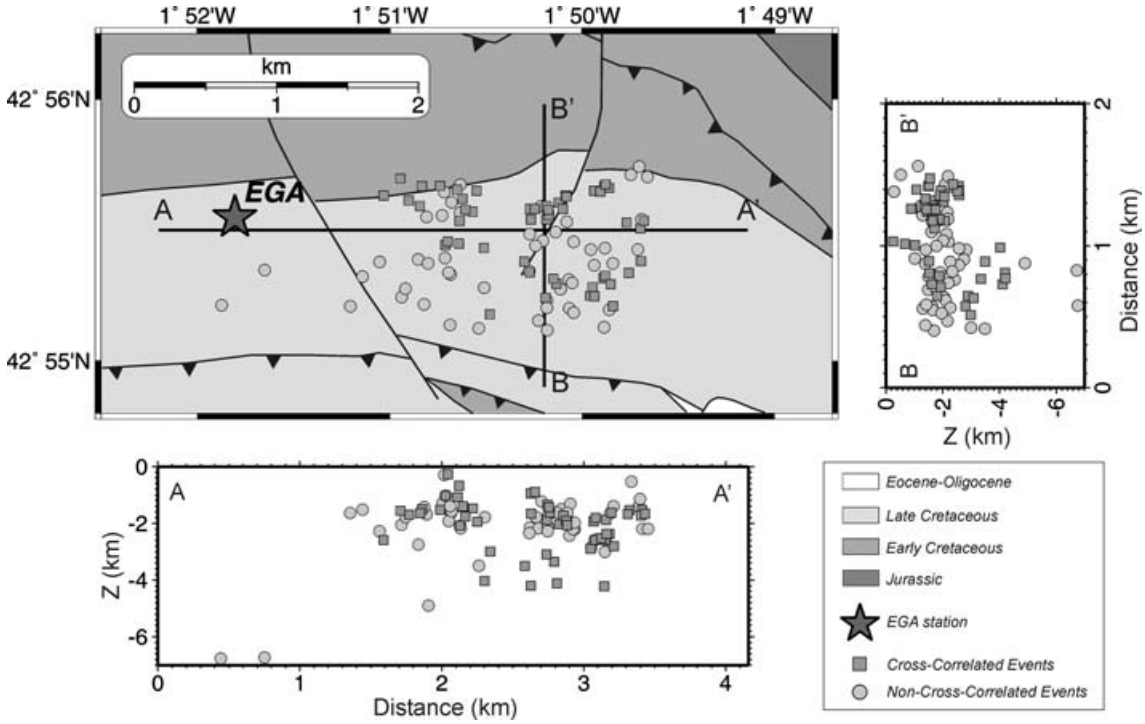

Figure 12. Relocation of the complete catalogue using the Double Difference approach. Squares show the cross-correlated events belonging to earthquake families, and circles the non-cross-correlated events.

Finally, the double difference approach was also applied to relocate the events not belonging to any of the defined families. Fig. 12 shows all the DD relocations. The epicentral area appears more clustered than with standard locations (Fig. 3a) and the E–W cross-section shows again the two sectors imaged with the clusters, events being mainly distributed between 1.5 and 2 km depth.

6 DISCUSSION AND CONCLUSIONS

The deployment of a temporary seismic network after the 2002 February 21 earthquake has provided new seismotectonic insights at the Basque–Cantabrian basin, on the western edge of the Pyrenees. Accurate relocation of the 13 aftershocks already recorded by permanent networks and hypocentral determinations of 93 previously unreported events provided relevant constraints on the properties of the seismically active area, the southern sector of the Aralar thrust unit.

The geographical location of the hypocentral area and the focal mechanisms obtained for the most significant events, showing normal fault solutions with one of the nodal planes roughly oriented E–W, both favour as the seismogenic structure the relaxation of the E–W thrusts that bounds the southern side of the Aralar thrusting system, activated by a dextral movement of the Egarrieta Fault, instead of other structures located nearby, like the Pamplona fault. The local stress field derived from focal solutions of the aftershocks shows maximum *P* directions oriented NW–SE. Although a homogeneous stress field for the whole Pyrenean range can not be defined from the present-day seismicity pattern of moderate magnitude (Nicolas *et al.* 1990; Delouis *et al.* 1993; Herraiz *et al.* 2000; Souriau *et al.* 2001), focal mechanisms of earthquakes occurred in the western part of the Pyrenees tend to suggest a NNW–SSE to NW–SE direction of maximum stress. The dips of the *P*-axes range from subhorizontal to subvertical, thus cases of normal or reverse faulting and a variable component of strike-slip are present in this region (Gagnepain *et al.* 1980; Gagnepain-Beyneix *et al.* 1982; Delouis *et al.* 1993; Souriau *et al.* 2001). Three focal solutions, coming from events with magnitudes between 4.2 and 4.9, are available for the 1982 seismic series, showing normal faulting with small strike-slip component and one of the nodal planes approximately E–W oriented (Olivera & Gallart 1987).

The seismotectonic relevance of the Aralar system revealed in this study could not be inferred from the sparse distribution of hypocentres shown in the catalogues established by permanent networks due to the low coverage of stations operating in this area. In these catalogues, the most active structure in this western Pyrenean area appears to be the central segment of the NNE–SSW oriented Pamplona fault. This fault is a crustal scale accident separating different tectonic domains and probably controlling the regional state of strain. The Aralar system is an E–W structure changing to NW–SE in its eastern edge when approaching the Pamplona fault, and corresponds to a secondary conjugate structure of this main fault. Therefore the shallow seismic activity detected and studied here may be explained in terms of relative movements affecting the whole fault system.

Statistical relations and aftershocks parameters were also established from the new data. A *P*-value of 0.9 resulted from the adjustment of the modified Omori law. This value, lying in the lower range of the expected values, reflects a moderate decay of the aftershock activity in this region. A local magnitude adjustment was also performed. The *b*-value of the cumulative Gutenberg–Richter distribution obtained, close to 0.8 and therefore relatively low, is characteristic of regions with concentrated seismicity and well-constrained fault planes. This solution agrees with the epicentral zone deduced from our data.

Further constraints on the hypocentral region have been obtained after a detailed analysis of the seismogram waveforms. First, a

correlation analysis has been applied to detect and associate events with similar waveforms. 10 clusters or families of earthquakes, containing a minimum of three events each, are obtained. The most significant differences between these families are the impulsive/emergent character of the first arrival, the relevance of an intermediate *P* phase arrival and the frequency content of the *S*-wave arrival. These differences have to be associated with differences in the rupture mechanisms and in the geographic hypocentral location. No remarkable temporal patterns were observed in the occurrence of the different families. Secondly, cross-correlation techniques, together with least-squares fitting of the relative arrival times have been applied to these event clusters, resulting in highly improved hypocentral locations. The final results, obtained with a double difference approach, show an E–W epicentral domain of only 2 km^2, where different rupture zones can be identified. The seismicity is mainly constrained to the 1.5–2.0 km depth range, although some deeper events may delineate a southward dip. The improved locations depict a narrower epicentral zone tightly clustered, and allow to associate as the seismogenic structure the E–W thrusts delineating the southern sector of the northward-verging Aralar thrusting slice.

The results obtained in this study enhance the importance of temporary monitoring by portable network deployments after a relevant earthquake, even of moderate magnitude. High-resolution aftershock experiments are needed to reveal the seismogenic features of areas poorly covered by permanent networks and provide invaluable constraints on the regional seismotectonics.

ACKNOWLEDGMENTS

This work was carried out with the support of the MARCONI (REN2001-1734) project from the Spanish MCYT. MR and CL benefited from a PhD grant from the Spanish MCYT. We would like to thank to the responsible of the IGN, RENASS, OMP and CEA databases for sharing the seismological data used in this study. We acknowledge Dr. A. Villaseñor for his numerous suggestions and comments. The authors also wish to thank Dr M. Herraiz and an anonymous reviewer for their constructive comments on this manuscript.

REFERENCES

Aster, R.C. & Scott, J., 1993. Comprehensive characterization of waveform similarity in microearthquake data sets, *Bull. seism. Soc. Am.,* **83**(4), 1307–1314.

Augliera, P., Cattaneo, M. & Eva, C., 1995. Seismic multiplets analysis and its implication in seismotectonics, *Tectonophysics,* **248,** 219–234.

Choukroune, P., 1992. Tectonic evolution of the Pyrenees, *Annu. Rev. Earth Planet. Sci.,* **20,** 143–158.

Delouis, B., Haessler, H., Cisternas, A. & Rivera, L., 1993. Stress tensor determination in France and neighbouring regions, *Tectonophysics,* **221,** 413–438.

Deichmann, N. & García-Fernández, M., 1992. Rupture Geometry from high-precision relative hypocentre locations of microearthquakes clusters, *Geophys. J. Int.,* **110,** 501–517.

Engeser, T. & Schwentke, W., 1986. Towards a new concept of the tectogenesis of the Pyrenees, *Tectonophysics,* **129,** 233–242.

Faci, E. *et al.*, 1997. Mapa geológico de Navarra, Escala 1:200.000. Gobierno de Navarra. Spain, p. 142.

Feuillée, P. & Rat, P., 1971. Structures et paléogéographies Pyrénéo-Cantabriques, in *Histoire Structurale du Golfe de Gascogne*, Vol. 1, pp. 1–48, eds Debyser, J., Le Pichon, X. & Montadert, L., Publ. Inst. Français du Pétrole, Ed. Technip.

Frémont, M.J. & Malone, S.D., 1987. High precision relative locations of earthquakes at Mount St. Helens, Washington, *J. geophys. Res.,* **92**(B10), 10 223–10 236.

Gagnepain, J., Mediano, T., Cisternas, A., Ruegg, J.C., Vadell, M., Hatzfeld, D. & Mezcua, J., 1980. Sismicité de la région d'Arette (Pyrénées-Atlantiques) et mécanismes au foyer, *Ann. Gefis.,* **36,** 499–508.

Gagnepain-Beyneix, J., Haessler, H. & Modiano, T., 1982. The Pyrenean earthquake of February 29, 1980: an example of complex faulting, *Tectonophysics,* **85,** 273–290.

García-Modéjar, J., 1996. Plate reconstruction of the Bay of Biscay, *Geology,* **24,** 635–638.

Goldstein, P., Dodge, D., Firpo, M. & Minner, L., 2003. SAC2000: Signal processing and analysis tools for seismologists and engineers. Invited contribution to 'The IASPEI International Handbook of Earthquake and Engineering Seismology', Vol. 81B, eds Lee, W.H.K., Kanamori, H., Jennings, P.C. & Kisslinger, C., Academic Press, London.

Goldstein, P. & Minner, L., 1996. SAC2000: Seismic signal processing and analysis tools for the 21st Century, *Seis. Res. Lett.,* **67,** 39.

Got, J.L., Fréchet, J. & Klein F.W., 1994. Deep fault plane geometry inferred from multiplet relative relocation beneath the south flank of Kilauea, *J. geophys. Res.,* **99**(B8), 15 375- 15 286.

Guo, Z. & Ogata, Y., 1997. Statistical relations between the parameters of aftershocks in time, space and magnitude. *J. geophys. Res.,* **102**(B2), 2857–2873.

Grandjean, G., Daignières, M., Gallart, J. & Hirn, A., 1994. Répartition de la sismicité dans la partie occidentale des Pyrénées. C.R. Acad. Sci. Paris, t. 319, série II, P. 527–533.

Hauksson, E. & Jones, L.M., 1989. The 1987 Whittier Narrows earthquake sequence in Los Angeles, Southern California: seismological and tectonic analysis, *J. geophys. Res.,* **94**(B7), 9569–9589.

Herraiz, M. *et al.*, 2000. The recent (upper Miocene to Quaternary) and present tectonic stress distributions in the Iberian Peninsula, *Tectonics,* **19,** 762–786.

Instituto Geológico y Minero de España (IGME), 1987. Serie Magna, Hoja Alsasua-114, (24–07) Escala 1:50.000. Mapa Geológico de España. Servicio de publicaciones del Ministerio de Indústria.

Instituto Geológico y Minero de España (IGME), 1978. Serie Magna, Hoja Gulina-115, (25–07) Escala 1:50.000. Mapa Geológico de España. Servicio de publicaciones del Ministerio de Indústria.

Kisslinger, C. & Jones, L.M., 1991. Properties of aftershock sequences in Southern California, *J. geophys. Res.,* **96**(B7), 11 947–11 958.

Larrasoaña, J.C., Parés, J.M., Millán, H., del Valle, J. & Pueyo, E.L., 2003. Paleomagnetic, structural, and stratigraphic constraints on traverse fault kinematics during basin inversion: the Pamplona fault (Pyrenees, North Spain), *Tectonics,* **22**(6), 1071, doi:10.1029/2002TC001446.

Lee, W.H.K., Bennet, R.E. & Meagher, K.L., 1972. A Method of estimating magnitude of local earthquakes from signal duration, US Geol. Surv. Open file report 1–28.

Lee, W.H.K. & Lahr, J.C., 1975. HYPO71 (revised): A computer program for determining hypocenters, magnitudes and first motion pattern of local earthquakes, US Geol. Surv. Open File report 75–311.

Martínez-Torres, L.M., 1989. El Manto de los Mármoles (Pirineo Occidental): geología estructural y evolución geodinámica. *PhD thesis*, Univ. País Vasco, Spain, p. 294.

Maurer, H. & Deichmann, N., 1995. Microearthquake cluster detection on waveform similarities, with an application to the western Swiss Alps, *Geophys. J. Int.,* **123,** 588–600.

Montadert, L., Charpal, O., Roberts, D.G., Guennoc, P. & Sibuet, J.C., 1979. Northeast Atlantic passive margins: rifting and subsidence processes, *Ammer. Geophys. Un. Revue,* **3,** 154–186.

Müller, J. & Rodgers, P., 1977. L'evolution des Pyrénées (domaine central et occidental). Le segment Hercynien, la chaine de fond alpine, *Geol. Alp.,* **53,** 141–191.

Nanjo, K., Nagama, H. & Sotomura, M., 1998. Rates of aftershock decay and the fractal structure of active fault systems, *Tectonophysics,* **287,** 173–186.

Nicolas, M., Santoire, J.M. & Delpech, P.Y., 1990. Intraplate seismicity: new seismotectonic data in Western Europe, *Tectonophysics,* **179,** 27–53.

Njike-Kassala, J.D., Souriau, A., Gagnepain-Beyneix, J., Martel, L. & Vadell, M., 1992. Frequency-magnitude relationship and Poisson's ratio in the Pyrenees, in relation to earthquake distribution, *Tectonophysics,* **215,** 363–369.

Ogata, Y., 1999. Seismicity analisis throught point-processs modeling: a review, *Pure appl. Geophys.,* **155,** 471–507.

Olivera, C. & Gallart, J., 1987. Sismicidad de la región de Navarra (Pirineos Occidentales), *Rev. de Geofísica,* **43,** 221–234.

Pedreira, D., Pulgar, J.A., Gallart J. & Díaz, J., 2003. Seismic evidence of Alpine crustal thickening and wedging from the Western Pyrenees to the Cantabrian Mountains (North Iberia), *J. geophys. Res.,* **108**(B4), 2204, doi:10.1029/2001JB001667.

Poupinet, G., Ellsworth, W.L. & Frechet, J., 1984. Monitoring velocity variations in the crust using earthquakes doublets: An application to the Calaveras Fault, California, *J. geophys. Res.,* **89**(B7), 5719–5731.

Rat, P., 1988. The Basque-Cantabrian basin between the Iberian and European plates; some facts but still many problems, *Rev. Soc. Geol. Esp.,* **1**(3–4), 327–348.

Reasenberg, P.A. & Oppenheimer, D., 1985. FPFIT, FPPLOT and FPPAGE: Fortran computer programs for calculating and displaying fault-plane solutions, US Geol. Surv. Open File report 85–739, p. 25.

Rubin, A.M., Gillard, D. & Got, J-L., 1999. Streaks of microearthquakes along creeping faults, *Nature,* **400,** 635–641.

Ruiz, M., Gallart, J., Díaz, J., Olivera, C., Pedreira D., López, C., González-Cortina, J.M. & Pulgar, J.A., 2006. Seismic Activity at the Western Pyrenean Edge, *Tectonophysics,* **412,** 217–235.

Saccorotti, G., Carmona, E., Ibáñez, J.M. & Del Pezzo, E., 2002. Spatial characterization of Agron, southern Spain, 1988–1989 seismic series, *Phys. Earth planet. Inter.,* **129,** 13–29.

Shearer, P.M., 1997. Improving local earthquake locations using the L1 norm and waveform cross correlation: application to the Whittier Narrows, California, aftershock sequence, *J. geophis. Res.,* **102**(B4), 8269–8283.

Souriau, A. & Pauchet, H., 1998. A new synthesis of Pyrenean seismicity and its tectonic implications, *Tectonophysics,* **290,** 221–244.

Souriau, A., Sylvander, M., Rigo, A., Fels, J.F., Douchain, J.M. & Ponsolles, C., 2001. Sismotectonique des Pyrénées: principales constraintes sismologiques. *Bull. Soc. Géol. France.*, **172,** 25–39.

Tsujiura, M., 1983. Characteristic frequencies for earthquake families and their tectonic implications: evidence from earthquake swarms in the Kanto District, Japan, *Pure appl. Geophys.,* **4,** 573–600.

Turcotte, D.L., 1992. *Fractals and Chaos in geology and geophysics*, Cambridge Univ. Press, New York, p. 221.

Turner, J.P., 1996. Switches in subduction direction and the lateral termination of mountain belts: Pyrenees-Cantabrian transition, Spain, *J. Geological Society,* **153,** 563–571.

Utsu, T., 1961. Statistical study on the ocurrence of aftershocks, *Geophys. Mag.,* **30,** 521–605.

Utsu, T., 1999. Representation and analysis of the earthquake size distribution: a historical review and some new approaches, *Pure appl. Geophys.,* **155,** 509–535.

Utsu, T., 2002. Statistical features of seismicity. Invited contribution to 'The IASPEI International handbook of earthquake and engineering seismology', Vol. 81A. Edited by Lee, W.H.K., Kanamori, H., Jennings, P.C. & Kisslinger, C. Academic Press, London.

Waldhauser, F., 2001. HypoDD—a program to compute double-difference hypocenter locations, US Geological Survey. Open File Report 01–113.

Waldhauser, F. & Ellsworth, W.L., 2000. A double-difference earthquake location algorithm: method an application to the northern Hayward fault, California, *Bull. seism. Soc. Am.,* **90**(6), 1353–1368.